Version of Record: https://www.sciencedirect.com/science/article/pii/S1359431122000758
Manuscript_a5784da9a85f970ed9939d793f33df8f

Modeling of Vapor-Liquid Interactions in Condensing Ejectors

Nanqiao Wang, Shanti Bhushan, Heejin Cho, Like Li*

Department of Mechanical Engineering
Mississippi State University, Mississippi State, MS 39762, USA

* Corresponding author: likeli@me.msstate.edu

Abstract

Ejectors are compact mechanical devices that utilize the expansion of a high-pressure primary fluid to entrain and compress a low-pressure secondary fluid by means of momentum transfer between the two streams of fluid. Condensing ejectors feature both momentum and heat transfer through the interaction between the vapor and liquid streams. The goal of this paper is to develop and validate a one-dimensional slug flow model to simulate the vapor-liquid interactions in two types of condensing ejectors – one with primary liquid and secondary vapor flows (Type I), and the other with primary vapor and secondary liquid flows (Type II). Control volume analysis of the mass, momentum, and energy balance in each phase and across the interface was conducted for the ejectors. The slug flow models for both types of ejectors are validated with published results in the literature. The friction coefficient on the inner wall of the ejectors and the interfacial heat transfer coefficient are identified as controlling parameters for the ejector performance in terms of pressure and temperature distributions along the axis. The detailed parametric study shows that the liquid inlet velocity and mixing tube diameter have a significant impact on the performance of the Type I ejectors, and the performance of the Type II ejectors is mainly controlled by the secondary liquid flow inlet temperature.

Keywords: Ejector; condensation; slug flow model; interfacial heat transfer.

1. Introduction

The ejector is a single-component compact mechanical device with two inlet flows of high and low pressures and one discharge of well mixed stream. The expansion of the high-pressure primary fluid will entrain and compress the low-pressure secondary fluid by momentum transfer, thus the ejector has a pump effect and has been widely applied in refrigeration systems [1] and thrust augmenting devices [2]. The condensing ejector (CE) is a special type of ejector involving vapor condensation, thus featuring both momentum and heat transfer through the interaction

© 2022 published by Elsevier. This manuscript is made available under the Elsevier user license
https://www.elsevier.com/open-access/userlicense/1.0/

between the vapor and liquid streams. Condensing ejectors can proficiently convert thermal energy to stagnation pressure, therefore it can be attractive for numerous applications, such as fluid metal magnetohydrodynamic cycles, Rankine cycles, and underwater propulsion systems. For instance, various Rankine cycle space power systems necessitate the fluid to condense into liquid after leaving the turbine and must operate in near zero gravity environment. This prevents the utilization of any conventional surface condenser and makes CE to be a suitable technology [3].

It is noted that for CEs with primary vapor and secondary liquid flows, the condensation behavior is similar to the direct contact condensation (DCC) of steam in supercooled water environment. The DCC is encountered in various industrial processes and applications, such as hybrid heat exchanger, warm degasification, and seawater desalination, with the advantages of high heat transfer coefficient and simple geometric structure of functional devices without any conductive medium [4,5]. These phenomena are also used in the field of nuclear engineering for system pressure, flow control and safety manage purposes, such as reactor cooling, pressure control in containment and reactor depressurization in case of emergency. The DCC of the steam stream released into the supercooling pool is likewise a powerful strategy to consolidate steam with high pressure and temperature without using any complex instruments. This thermal-hydraulic phenomenon is of great significance in nuclear, chemical, and marine engineering applications [6–11]. Song et al. [6] experimentally investigated the DCC phenomena by discharging steam jets into a subcooled pool water with various parameter settings. Song et al. [5] also discussed the characteristics of condensed steam jet according to experimental measurements and direct visual observation.

In the past several decades, many theoretical and numerical studies have been conducted to understand the interactions between the primary and secondary flows within the various sections for ejector design, performance prediction and optimization. Keenan et al. [12] proposed a widely used 1D analysis for jet pumps and ejectors with the constant-pressure mixing theory, which assumes that the primary and secondary flows are mixed under constant pressure in the mixing tube. Munday and Bagster [13] proposed a new theory that first considered the discreteness of the primary and secondary flows; the performance of the ejector was predicted and verified by both literature results and plant-scale tests. Eames et al. [14], Sun and Eames [15] and Sun et al. [16] modified Keenan's model to analyze a small-scale steam ejector. Their models were not robust enough to analyze the complex fluid flow in the ejector, and the theoretical values are always

higher than the test results. Huang et al. [8] further improved the 1D model to analyze the performance of the ejector at the critical operation mode when both the primary and secondary jets are chocking; then the model was verified by experimental data. Ouzzane and Aidom [9] developed a similar 1D model for a constant-pressure mixing ejector and the effect of operation condition and geometric changes on the ejector performance was also studied.

A 1D model was also used by Rogdakis et al. [17] to study the ejector performance using high pressure ammonia vapor as the primary fluid. A parametric study was carried out under various operating conditions. Sun [16] studied the effect of ejector geometry on their performance based on a 5kW steam jet refrigerator and provided valuable experimental data for future comparison. Compared with the fixed-geometry ejector, the variable-geometry ejector cycle can achieve optimum performance under various operating conditions. An axisymmetric CFD model was developed by Varga et al. [18] to evaluate the performance of a steam ejector. The study found that the ejector performance is related to geometric parameters of the ejector suction, mixing and diffuser sections and the operating conditions. Their results also showed the existence of an optimal nozzle throat to mixing section area ratio. Ma et al. [19] designed and experimentally tested a novel steam ejector refrigerator suitable for solar energy applications with a moveable spindle based on the previous 1D CFD model and optimized geometric parameters [18]. They showed that the best performance of the ejector can be achieved by fine-tuning the spindle in controlling the primary flow. Liu et al. [20] presented a two-phase flow ejector model including sub-models of motive nozzle flow, suction nozzle flow, mixing section flow and diffuser flow to determine the efficiencies of internal ejector components in refrigeration cycles. They implemented empirical correlations into a CO_2-based air conditioning system model and estimated the ejector component efficiencies at different ejector geometries and operating conditions. Chunnanond and Aphornratana [21] measured the static pressure profile along a 3kW steam ejector refrigerator at various operating conditions, then further performed a parametric study by introducing expansion angle, effective position and shock position. By adjusting these three geometrically related parameters, the performance of the ejector can be optimized. Based on the flow governing equations and thermodynamics Landoulsi et al. [22] proposed a 1D constant-area model of the ejector. Then carried out a parametric study to optimize the system performance. The results show that the geometric parameters have a great influence on the overall performance. Tashtoush et al [23] pinpointed that the cross-section area ratio of the mixing tube and the primary

nozzle (ejector area ratio) has a significant impact on the cycle performance according to the 1D thermodynamic model.

In addition to 1D models, more computationally expensive 2D and 3D computational fluid dynamics (CFD) models have also been proposed to study ejectors. Riffat et al. [24] investigated the steam ejector heat pumps by 3D CFD analysis. They pointed out the influence of the ejector nozzle geometry and position on the performance, showing that CFD has the potential to optimize the ejector design. As one of the first research works on CFD models, Colarossi et al. [11] proposed a 2D CFD model for a two-phase flow (primary vapor and secondary liquid flows) through a CE with carbon dioxide as the working fluid. Wang et al. [10] developed a 2D CFD model studying the patterns of primary flow jet core in a steam ejector at different operating conditions. Recently, Dong et al. [25] investigated the effect of the mixing tube length on the steam ejector performance under different operating and geometric parameters using a 3D CFD simulation. The results show that the critical back pressure first increases and then decreases with the increase of the mixing region length. Therefore, to achieve the optimal performance of the ejector, the length of the mixing tube should be optimized accordingly.

The above literature review indicates that most of the previous models were proposed for ejectors with both the primary and secondary flows in the vapor phase without condensation; for those involving condensation, 2D or 3D CFD models were typically applied; furthermore, all the models were proposed for specific ejector configurations with either primary-vapor secondary-liquid or primary-liquid secondary-vapor flows. A computationally efficient 1D model that can simulate the vapor-liquid interactions and predict the performance of condensing ejectors with both primary-vapor secondary-liquid and primary-liquid secondary-vapor flows would be valuable for CEs design and optimization with applications in refrigeration cycles and for chemical/nuclear reactors cooling.

Hence, in this paper we propose a general 1D slug-flow model for two CE configurations (Type I with primary-liquid secondary-vapor flows and Type II with primary-vapor secondary-liquid flows) with focus on their heat transfer and pressure change performance. Control volume analysis for the mass, momentum, and energy balance in the different phases as well as on the vapor-liquid interface was conducted. The 1D slug-flow model is validated with published results for both types of CEs and then applied to study the effects of the various geometric and operational parameters. In the remainder of this paper, Section 2 introduces the configurations of the two types

of CEs; Section 3 presents the detailed control volume analysis for both types of CEs; verification and validation of the models are provided in Section 4; Section 5 presents the parametric study for generic ejectors under various operation conditions and geometry parameters; and conclusions are given in Section 6.

2. Condensing Ejector Configurations

An ejector is typically composed of two fluid streams interacting within three regions along its axis. For the condensing ejectors studied in this work, a subcooled liquid stream and a vapor stream interact with each other to produce a mixed stream at the exit in liquid phase. The stagnation pressure at the condensing ejector exit can be higher than that of both inlet streams when controlled by a back-pressure control valve [3]. The three regions include an inlet region with two convergent nozzles (also called a suction chamber [8]) where the two inlet streams come into contact, a mixing section for sufficient liquid-vapor mixing (usually with constant-area [3] or constant-pressure mixing [8]), and a diffuser through which the mixed liquid is exhausted. The fluid flow along the centerline of the CE is called the primary flow and the other in the annulus of the inlet region the secondary (suction) flow. In this work, both types of CEs with primary liquid and primary steam streams will be investigated, with more details described in the following.

Figure 1 shows the schematic of the two types of CEs. Also, the Type I ejector with primary liquid and secondary vapor flows studied in [3] is shown in Fig. 2. It should be noted that in this work we focus on the analysis within the mixing section of constant area. The control volumes (CV) selected for thermodynamic analysis for both types of ejectors and the velocity and temperature profiles within the mixing region are sketched in Fig. 3.

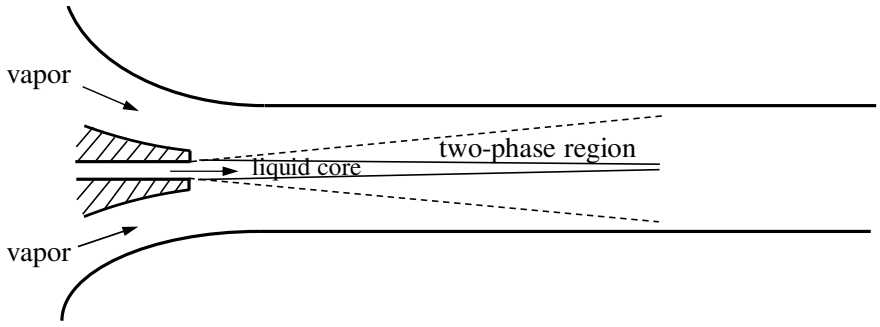

(a)

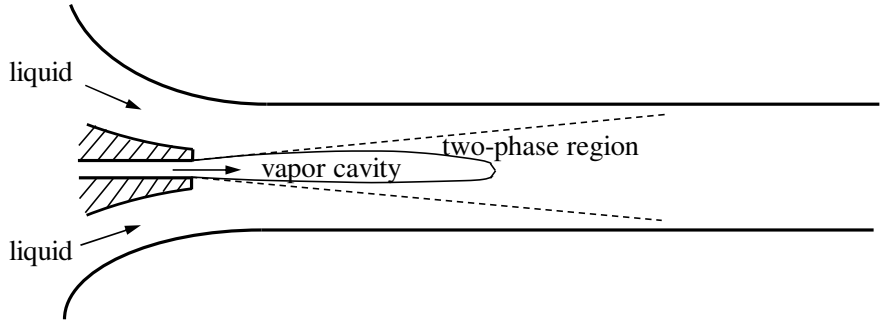

(b)

Fig. 1 Schematic depiction of the ejectors with vapor condensation and (a) primary liquid flow and secondary vapor flow, and (b) primary vapor flow and secondary liquid flow.

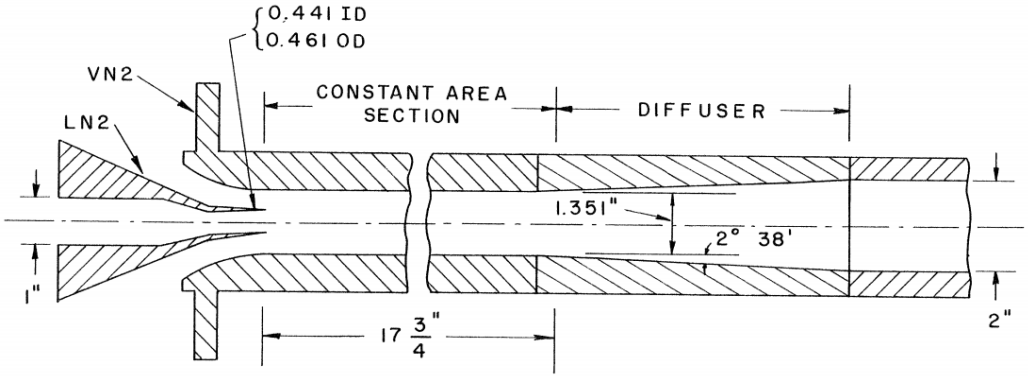

Fig. 2 Geometric configuration of the ejector studied in [3] with primary liquid and secondary vapor flows.

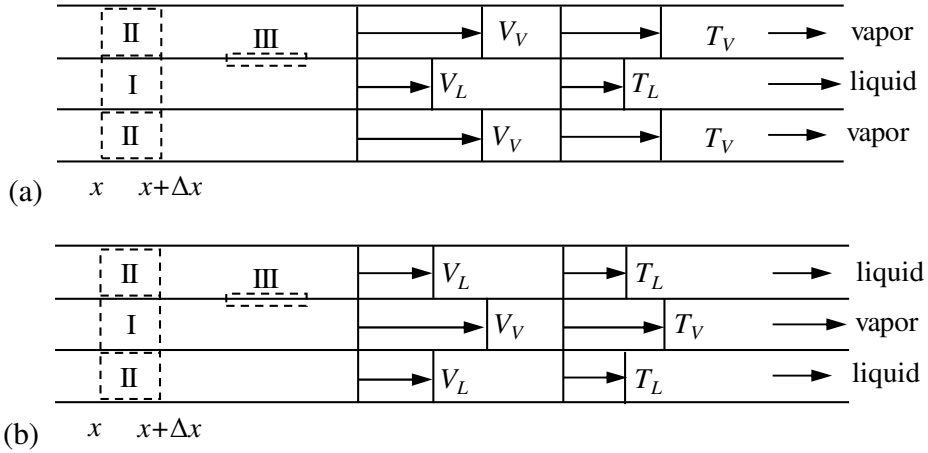

Fig. 3 Control volumes I, II and III, velocity and temperature profiles for the slug model for the ejectors with (a) primary liquid flow and secondary vapor flow, and (b) primary vapor flow and secondary liquid flow.

3. Control Volume Analysis

In this section, the details of the slug flow model for both types of ejectors depicted in Fig. 1 will be presented. The main assumptions for the 1D slug flow model include [3,20]: (1) the flow is steady, (2) the flow velocity and temperature within both liquid and vapor regions are 1D with uniform profiles (see Fig. 3), (3) the static pressure is also 1D and uniform in each axial location (i.e., the static pressure is the same within the liquid and vapor regions), (4) the drag and shear stress at the vapor-liquid interface are assumed zero and the condensate crosses the interface with a tangential velocity equal to the local vapor velocity, (5) the dominant heat transfer is from the interface to the liquid region, while the heat transfer from the vapor region to the interface is negligible, (6) heat transfer through the tube wall and axial conduction are also negligible, and (7) the liquid is incompressible, the vapor is saturated or slightly superheated, and the vapor-liquid interface temperature is equal to the saturation temperature corresponding to the local static pressure. With those assumptions, the mass, momentum, and energy conservation equations can be derived within the CVs shown in Fig. 2 following the CV analysis in [3]. And the numerical method for solving those equations will also be summarized.

3.1 Conservation Equations

3.1.1 Ejectors with Primary Liquid and Secondary Vapor Flows

For the ejector with primary liquid flow and secondary vapor flow, the conservation equations for the CVs I and II in Fig. 2a include:

Mass equation:

$$d\left(\rho_V V_V A_V\right) = -\dot{m}_c, \tag{1a}$$

$$\rho_L d\left(V_L A_L\right) = \dot{m}_c, \tag{1b}$$

where the subscripts, V and L, denote the vapor and liquid phases, respectively, ρ is the density, V is the velocity, $\dot{m}_c$ is the mass flow rate of condensate crossing the vapor-liquid interface from x to $x+\Delta x$, and the areas can be calculated as $A_L = \pi r_L^2$ and $A_V = \pi\left(R_w^2 - r_L^2\right)$ with r_L the inner radius of the primary liquid nozzle and R_w the radius of duct.

Momentum equation:

$$d\left(\rho_V V_V^2 A_V\right) + A_V dp = -\dot{m}_c V_V - F_w, \tag{2a}$$

$$\rho_L d\left(V_L^2 A_L\right) + A_L dp = \dot{m}_c V_V, \tag{2b}$$

where p is the static pressure, the wall shear force is $F_w = 2\pi R_w \Delta x \tau_w$ with τ_w the shear stress.

Energy equation:

$$d\left[\rho_V V_V A_V \left(h_V + \frac{V_V^2}{2}\right)\right] = -\dot{m}_c \left(h_V + \frac{V_V^2}{2}\right), \tag{3a}$$

$$\rho_L d\left[V_L A_L \left(h_L + \frac{V_L^2}{2}\right)\right] = \dot{m}_c \left(h_V + \frac{V_V^2}{2}\right). \tag{3b}$$

The energy balance for CV III is used to relate $\dot{m}_c$ to the interfacial heat transfer coefficient h through

$$\dot{Q}_L = \dot{m}_c \left(h_V - h_L + \frac{V_V^2 - V_L^2}{2}\right), \tag{4}$$

$$h = \frac{\dot{Q}_L}{2\pi r_L \Delta x \left(T_{\text{sat}} - T_L\right)}, \tag{5}$$

where $\dot{Q}_L$ is the heat transfer rate from the vapor-liquid interface to the liquid core, h_V and h_L are respective specific enthalpies, and T_{sat} is the saturated temperature corresponding to the local static pressure.

3.1.2 Ejectors with Primary Vapor and Secondary Liquid Flows

For ejectors with primary vapor flow and secondary liquid flow as shown in Fig. 1b, the conservation equations for the CVs in Fig. 2b can be similarly obtained:

Mass equation:

$$d\left(\rho_V V_V A_V\right) = -\dot{m}_c, \tag{6a}$$

$$\rho_L d\left(V_L A_L\right) = \dot{m}_c, \tag{6b}$$

where the areas become $A_V = \pi r_V^2$ and $A_L = \pi\left(R_w^2 - r_V^2\right)$ with r_V the inner radius of the primary vapor nozzle.

Momentum equation:

$$d\left(\rho_V V_V^2 A_V\right) + A_V dp = -\dot{m}_c V_V, \tag{7a}$$

$$\rho_L d\left(V_L^2 A_L\right) + A_L dp = \dot{m}_c V_V - F_w, \tag{7b}$$

where the shear stress τ_w is between the wall and the annular liquid.

Energy equation:

$$d\left[\rho_V V_V A_V\left(h_V + \frac{V_V^2}{2}\right)\right] = -\dot{m}_c\left(h_V + \frac{V_V^2}{2}\right), \tag{8a}$$

$$\rho_L d\left[V_L A_L\left(h_L + \frac{V_L^2}{2}\right)\right] = \dot{m}_c\left(h_V + \frac{V_V^2}{2}\right). \tag{8b}$$

The energy balance for CV III and the interfacial heat transfer coefficient are

$$\dot{Q}_L = \dot{m}_c\left(h_V - h_L + \frac{V_V^2 - V_L^2}{2}\right), \tag{9}$$

$$h = \frac{\dot{Q}_L}{2\pi r_V \Delta x\left(T_{\text{sat}} - T_L\right)}, \tag{10}$$

where $\dot{Q}_L$ is the heat transfer rate from the vapor-liquid interface to the liquid annulus.

3.2 Numerical Method for Constant Area Duct

For vapor-liquid flow in a constant area duct, the conservation equations for both types of ejectors in Eqs. (1-5) and (6-10) can be rearranged to yield the following:

$$c_{12} d\rho_V + c_{13} dp = \gamma_1, \tag{11}$$

$$c_{22} dp + c_{23} dh_L = \gamma_2, \tag{12}$$

$$c_{32} d\rho_V + c_{33} dh_V + c_{34} dp = \gamma_3, \tag{13}$$

$$h_V = h_V\left(\rho_V, p\right), h_L = h_L\left(T_L\right), \tag{14}$$

$$dA_L = \left(\beta_1 - b_{13}dp\right)/b_{11},\ dA_V = -dA_L, \tag{15}$$

$$dV_L = \left(\alpha_1 - a_{11}dA_L\right)/a_{13}, dV_V = \left(\alpha_2 - a_{21}dA_L - a_{25}d\rho_V\right)/a_{24}, \tag{16}$$

where the coefficients include

$$\begin{aligned} &c_{12} = -A_V V_V^2, c_{13} = A_V + A_L \frac{\rho_V V_V^2}{\rho_L V_L^2}, c_{22} = -A_L V_L, \\ &c_{23} = \rho_L A_L V_L, c_{32} = -A_V V_V^3, c_{33} = \rho_V A_V V_V, c_{34} = A_L \frac{\rho_V V_V^3}{\rho_L V_L^2} \end{aligned} \tag{17}$$

$$\begin{aligned} &a_{11} = \rho_L V_L, a_{13} = \rho_L A_L, a_{21} = -\rho_V V_V, a_{24} = \rho_V A_V, a_{25} = A_V V_V, \\ &b_{11} = -\rho_L V_L^2, b_{13} = A_L, \alpha_1 = \dot{m}_c, \alpha_2 = -\dot{m}_c \end{aligned} \tag{18}$$

For type I ejectors with primary liquid flow and secondary vapor flow, the remaining terms are

$$\begin{cases} \beta_1 = \dot{m}_c \left(V_V - 2V_L\right) \\ \gamma_1 = -F_w + \dot{m}_c V_V + \dot{m}_c \dfrac{\rho_V V_V^2}{\rho_L V_L^2}\left(V_V - 2V_L\right) \\ \gamma_2 = \dot{m}_c \left[h_V - h_L + \dfrac{\left(V_V - V_L\right)^2}{2}\right] \\ \gamma_3 = \dot{m}_c \left[V_V^2 + \left(V_V - 2V_L\right)\dfrac{\rho_V V_V^3}{\rho_L V_L^2}\right] \end{cases} \tag{19}$$

While for type II ejectors with primary vapor flow and secondary liquid flow, those terms read

$$\begin{cases} \beta_1 = \dot{m}_c \left(V_V - 2V_L\right) - F_w \\ \gamma_1 = \dot{m}_c V_V + \dot{m}_c \dfrac{\rho_V V_V^2}{\rho_L V_L^2}\left(V_V - 2V_L - \dfrac{F_w}{\dot{m}_c}\right) \\ \gamma_2 = \dot{m}_c \left[h_V - h_L + \dfrac{\left(V_V - V_L\right)^2}{2}\right] + V_L F_w \\ \gamma_3 = \dot{m}_c \left[V_V^2 + \left(V_V - 2V_L - \dfrac{F_w}{\dot{m}_c}\right)\dfrac{\rho_V V_V^3}{\rho_L V_L^2}\right] \end{cases} \tag{20}$$

To close and solve the system of equations, the equation of state for either superheated or saturated vapor (with mixture vapor quality q) can be used:

Superheated vapor:

$$h_V = h_V\left(p, T_V\right) \text{ and } \rho_V = \rho_V\left(p, T_V\right) \text{ or} \tag{21}$$

Saturated vapor:

$$h_V = h_V\left(p, q\right) \text{ and } \rho_V = \rho_V\left(p, q\right) \tag{22}$$

Specifically, Eqs. (11-13) can be rearranged as

$$c_{12}\rho_V\left(p, T_V\right)\big|_{x+\Delta x} + c_{13}p\big|_{x+\Delta x} = \gamma_1 + c_{12}\rho_V\big|_x + c_{13}p\big|_x \tag{23}$$

$$c_{22}p\big|_{x+\Delta x} + c_{23}h_L\left(T_L\right)\big|_{x+\Delta x} = \gamma_2 + c_{22}p\big|_x + c_{23}h_L\left(T_L\right)\big|_x \tag{24}$$

$$\begin{aligned} &c_{32}\rho_V\left(p, T_V\right)\big|_{x+\Delta x} + c_{33}h_V\left(p, T_V\right)\big|_{x+\Delta x} + c_{34}p\big|_{x+\Delta x} = \\ &\gamma_3 + c_{32}\rho_V\big|_x + c_{33}h_V\big|_x + c_{34}p\big|_x \end{aligned} \tag{25}$$

Hence, for superheated vapor, Eqs. (21, 23, 25) can be solved by iteration to obtain p, T_V, h_V, ρ_V at $x+\Delta x$ based on the given information at x; and for saturated vapor, Eqs. (22, 23, 25) can be similarly solved to obtain p, q, h_V, ρ_V at $x+\Delta x$. These can then be substituted into Eqs. (24, 15, 16) to determine h_L, T_L, A_L, A_V, V_L and V_V at $x+\Delta x$. In the ejectors, the boundary conditions at $x = 0$ can be obtained from the operating conditions, thus a marching process can be used to solve all the variables along the ejector axis.

It should be noted that analytical relations are needed for the vapor state equations (24, 25), in this work we use the relations developed in [26]

$$\rho_V = 1000\left(\frac{4.55504T}{p} + B\right)^{-1} \text{ in kg/m}^3 \tag{26a}$$

with

$$\begin{aligned} &B = B_0 + B_0^2 g_1(\tau)\tau p + B_0^4 g_2(\tau)\tau^3 p^3 - B_0^{13} g_3(\tau)\tau^{12} p^{12}, \\ &(\tau = T^{-1},\ p \text{ in atm}), \\ &B_0 = 1.89 - 2641.62\tau \times 10^{80870\tau^2} \\ &g_1(\tau) = 82.546\tau - 1.6246\times 10^5 \tau^2 \\ &g_2(\tau) = 0.21828 - 1.2697\times 10^5 \tau^2 \\ &g_3(\tau) = 3.635\times 10^{-4} - 6.768\times 10^{64}\tau^{24} \end{aligned} \tag{26b}$$

and

$$h_V = F_0 p + \frac{F_1}{2} p^2 + \frac{F_3}{4} p^4 + \frac{F_{12}}{13} p^{13} + F', \text{ in kJ/kg} \tag{27a}$$

with

$$\begin{aligned}
&F_0 = \frac{\partial(\tau B_0)}{\partial \tau} \\
&F_{1,3,12} = \frac{\partial(\tau \phi_{1,3,12})}{\partial \tau} \\
&\phi_1 = B_0^2 g_1(\tau)\tau, \phi_3 = B_0^4 g_2(\tau)\tau^3, \phi_{12} = -B_0^{13} g_3(\tau)\tau^{12}, \\
&F' = 1.4720(T - T_0) + 3.7783\times10^{-4}\left(T^2 - T_0^2\right) + \\
&47.8365\ln(T/T_0) + 2502.36, T_0 = 273.15\text{K}
\end{aligned} \tag{27b}$$

Finally, the Newton's method is implemented to iteratively solve the nonlinear system of equations (21, 23, 25) or (22, 23, 25) that can be written in the general form as f_i (**x**) = 0 with (i = 1 ~ 4)

$$\mathbf{x}_{n+1} = \mathbf{x}_n - \mathbf{G}^{-1}\mathbf{f}(\mathbf{x}_n) \tag{28}$$

where $\mathbf{x} = (p, T_V, h_V, \rho_V)^{\mathrm{T}}$ for superheated vapor, and $\mathbf{x} = (p, q_V, h_V, \rho_V)^{\mathrm{T}}$ for saturated vapor, and **G** is the Jacobian matrix defined as

$$\mathbf{G} = \begin{bmatrix} \partial f_1/\partial x_1 & \partial f_1/\partial x_2 & \partial f_1/\partial x_3 & \partial f_1/\partial x_4 \\ \partial f_2/\partial x_1 & \partial f_2/\partial x_2 & \partial f_2/\partial x_3 & \partial f_2/\partial x_4 \\ \partial f_3/\partial x_1 & \partial f_3/\partial x_2 & \partial f_3/\partial x_3 & \partial f_3/\partial x_4 \\ \partial f_4/\partial x_1 & \partial f_4/\partial x_2 & \partial f_4/\partial x_3 & \partial f_4/\partial x_4 \end{bmatrix} \tag{29}$$

An in-house computational code was developed to iteratively solve the system of equations. A convergence criterion for the relative L_2-norm error, E_2, between $\mathbf{x}_{n+1}$ and $\mathbf{x}_n$ with $E_2 < 10^{-10}$ was used for all nodes. Detailed model verification and validation will be presented in the next section.

4. Model Verification and Validation

The reported experimental and model results in [3] will be used here to verify and validate our model for ejectors with primary liquid and secondary vapor flows. For the second type of ejectors with primary vapor and secondary liquid flows, the reported data in the literature is rather limited, and we will use the results in [5,6] to validate our model.

4.1 Ejectors with Primary Liquid and Secondary Vapor Flows

The Type I ejector selected for model verification and validation is depicted in Fig. 2. It is worth mentioning that the inner diameter of the primary liquid nozzle of the test section is 11.2 mm (0.441 inch) as seen in Fig. 2, so that r_{L0} = 5.6 mm; while for the detailed modeling results presented in [3], the inner diameter r_{L0} = 5.72 mm (0.225 inch) was chosen. Examination of the two sets of results using the present model shows that those two dimensions would give very similar results. To show an in-depth comparison with the results in [3], the simulation results shown below were all obtained from using r_{L0} = 5.72 mm. Specifically, Figs. 4-8 show the variations of the static pressure, vapor and liquid temperatures, condensation rate, vapor flow rate and Mach number, and liquid jet velocity and radius along the ejector axial direction. In each figure, the effect of the liquid-vapor interfacial heat transfer coefficient h (W/m^{2}K) can be clearly observed; P_{0g} in Fig. 4 denotes the upstream vapor tank pressure, and experimental data collected from three independent runs conducted on the same ejector were also included. The excellent agreement in Figs. 4-8 demonstrates that the present model is very accurate for all the variables examined. More importantly, the modeling results for only the first 0.10 or 0.25 mm were presented in [3], while the present model can be used to simulate the results within the entire 450 mm mixing region, confirming the reliability of the present model. It is noteworthy that Fig. 4 shows the dependence of static pressure on h, so it is necessary to appropriately adjust the value of h as an axial function [3]. This is also the reason that present model fits well with the reference model but is different from the experimental data. Detailed analysis will be carried out in Section 5.

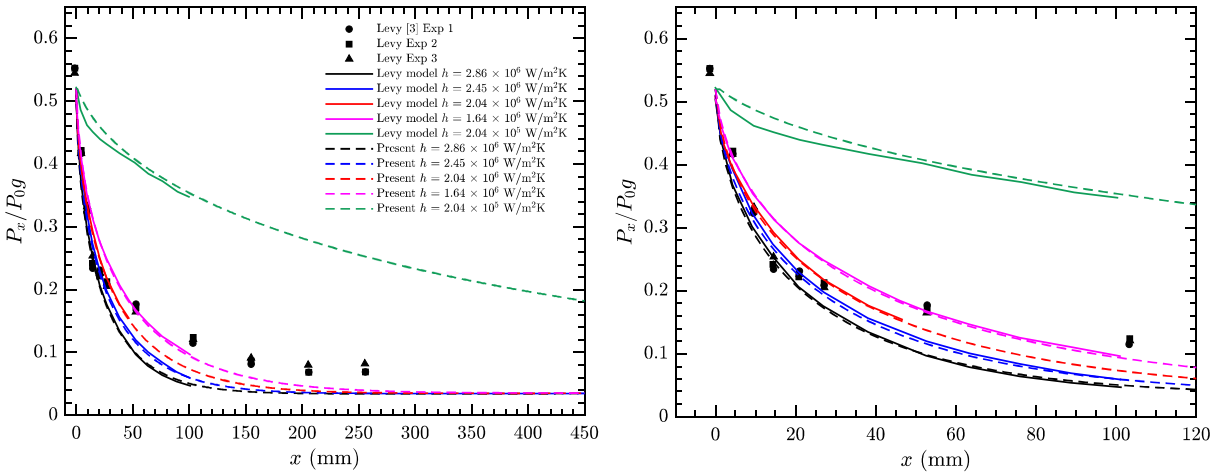

Fig. 4 Static pressure distribution along the ejector axis (a) in the entire 450 mm constant-area mixing region, and (b) zoom-in view at the first 120 mm entrance length with different interfacial heat transfer coefficient.

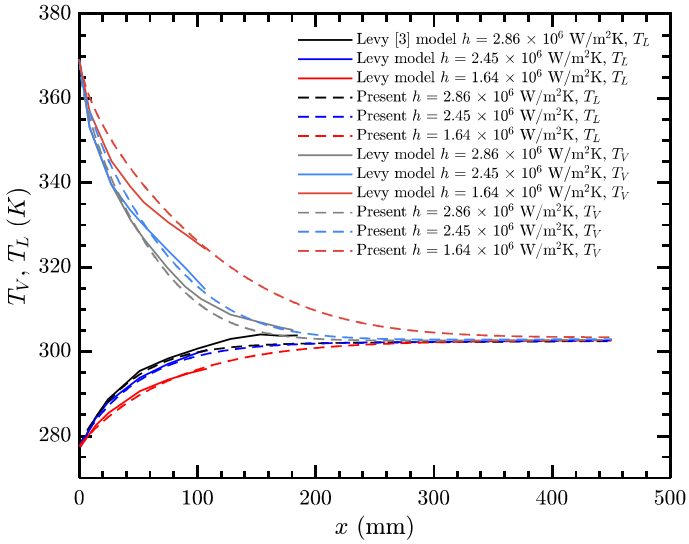

Fig. 5 Vapor and liquid temperature profiles along the ejector axis with different interfacial heat transfer coefficient.

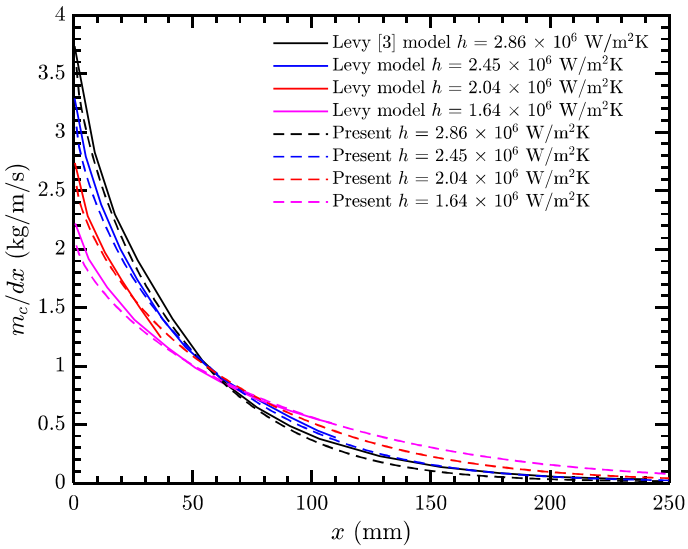

Fig. 6 Condensation rate distribution at the first 250 mm entrance length with different interfacial heat transfer coefficient.

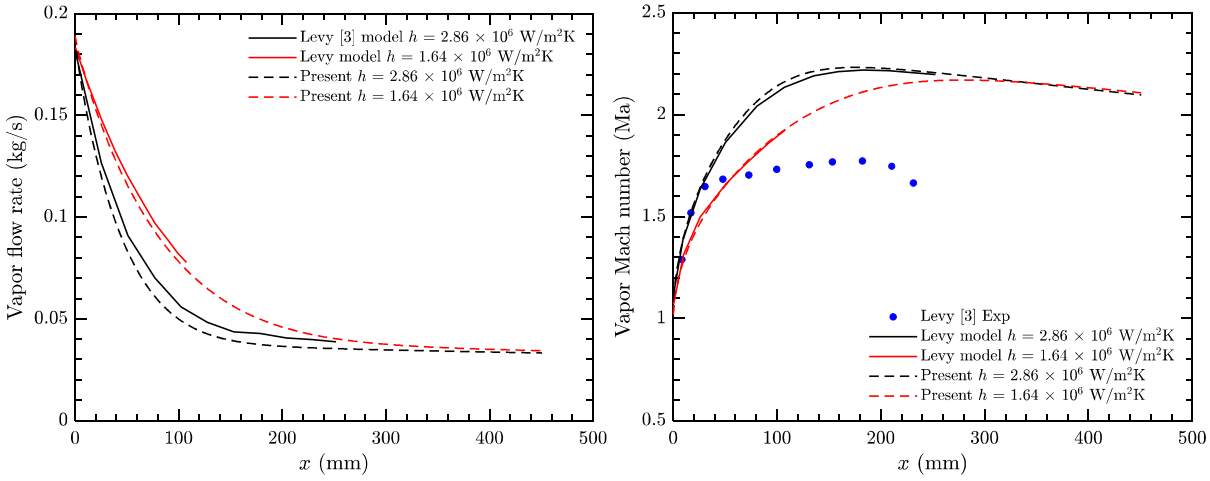

Fig. 7 (a) Vapor flow rate and (b) Mach number distributions along the ejector axis with different interfacial heat transfer coefficient.

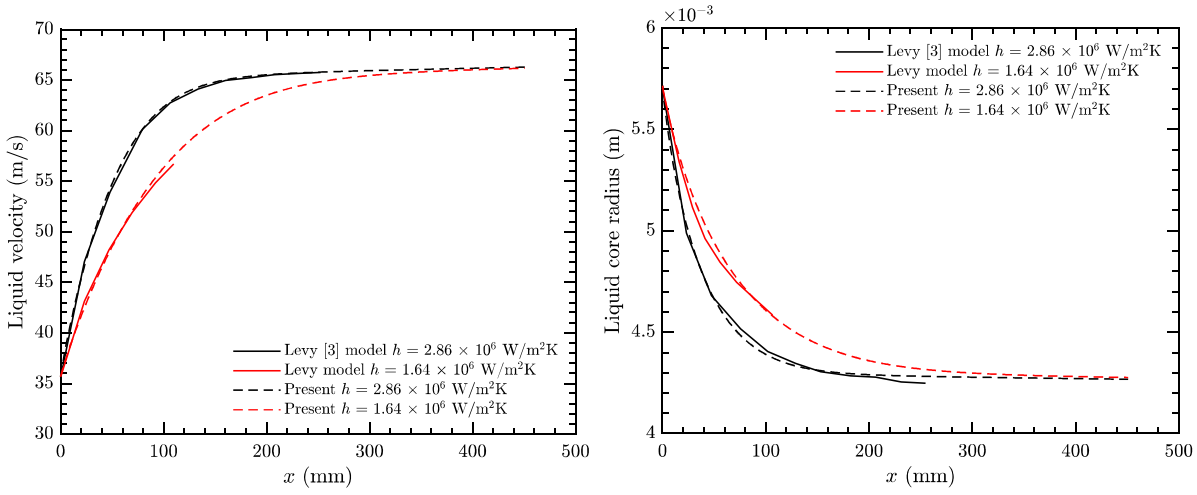

Fig. 8 (a) Liquid jet velocity and (b) liquid jet radius variations along the ejector axis with different interfacial heat transfer coefficient.

4.2 Ejectors with Primary Vapor and Secondary Liquid Flows

For Type II ejectors with primary vapor flow and secondary liquid flow, a detailed literature survey has been conducted, however, the published results in the literature are very rare. Here, we use the available results for the centerline vapor temperature in [5,6] for validation of our slug flow model. Although the ejector configuration in [5,6] is for vapor jet entering liquid pools and it is not exactly the same as the Type II ejectors with secondary liquid flows, this represents the closely related published results available. A careful examination of the reported data in [5,6] also confirms that the vapor temperature profile is controlled by the liquid pool temperature and insensitive to the vapor nozzle size or vapor flow rate. Therefore, it is assumed that when the area of the secondary liquid flow at the inlet is large enough compared to the primary vapor flow area, the results from the present Type II ejector model would be able to mimic the vapor temperature drop in the liquid pool. For demonstration, Fig. 9 shows the vapor temperature profiles with four different liquid flow temperatures (T_1 = 20 ºC, T_2 = 30 ºC, T_3 = 40 ºC, T_4 = 50 ºC) at the inlet. The other main simulation parameters include Ma_0 = 2.0, P_{0g} = 172.37 kPa, T_{V0} = 388.15 K, V_{L0} = 36.58 m/s, h_{int} = 0.41 MW/m^{2}K, and f = 0.0001.

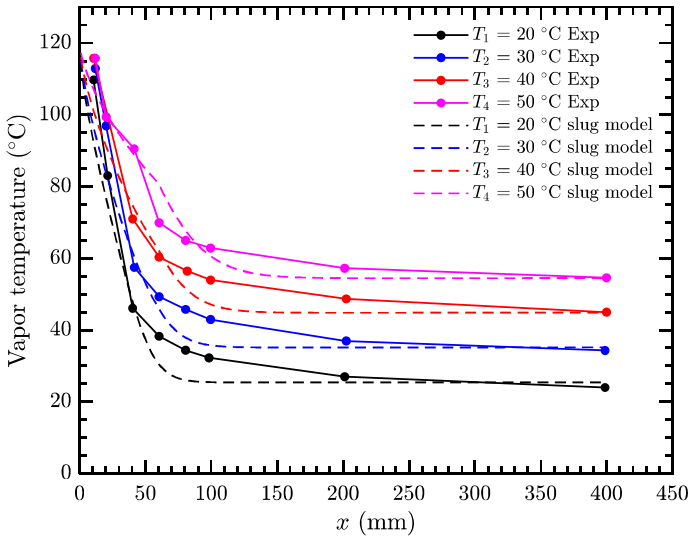

Fig. 9 Comparison of the centerline vapor temperature along the ejector axis at different secondary liquid flow temperatures.

Considering all the uncertainties involved in the simulation parameters, the overall comparison is quite encouraging as seen in Fig. 9. Good agreement is noticed in the region near the vapor nozzle inlet (x < 100 mm); and the same converged values are observed for each case in Fig. 9. In addition, the present slug flow model showed faster convergence toward the asymptotic value compared to the experimental result for each case. The mean absolute errors for the centerline vapor temperature from the slug flow mode are 6.7 ºC, 7.0 ºC, 5.2 ºC, and 3.8 ºC for the respective cases with T_1 = 20 ºC, T_2 = 30 ºC, T_3 = 40 ºC, and T_4 = 50 ºC. Future improvement can be pursued with varying heat transfer coefficient along the ejector axis. This will be further studied in the next section with a detailed parametric study.

5. Parametric Study for Generic Ejectors

5.1 Ejectors with Primary Liquid and Secondary Vapor Flows

5.1.1 Effect of Interfacial Heat Transfer Coefficient

Here, different from the previous consideration that the vapor-liquid interface heat transfer coefficient is constant in the entire ejector geometry, we adjust it to the varying parameter as a function of axial position. Specifically, for the first test, the heat transfer coefficient h_1 is set equal to 2.45 MW/m^{2}K in the range 0 < x < 25.4 mm, to 1.02 MW/m^{2}K from 25.4 < x < 152.4 mm, and to 0.31 MW/m^{2}K for x > 152.4 mm with V_L = 35.66 m/s (117 fps). For the second test with V_L =

19.51 m/s (64 fps), h_2 = 2.04, 0.72, and 0.02 MW/m^{2}K are used in the range 0 < x < 25.4 mm, 25.4 < x < 190.5 mm, and x > 190.5 mm, respectively. Fig. 10 shows the comparison of normalized static pressure along the ejector axis at different liquid inlet velocities. Very good agreement with the experiment data [3] can be observed for the two tests; the mean absolute errors of the normalized static pressure are 0.0134 for the first test with three sets of experimental data and 0.0148 for the second test with two sets of experimental data, respectively. Then we further investigated the effect of varying heat transfer coefficient on the vapor Mach number. We rerun the case shown in Fig. 7(b) with the same varying h_1 set as in the first test. As shown in Fig. 11, the vapor Mach number results match perfectly with the reference model [3] and the modeling results with varying h_1 show better agreement with the experimental data compared to the previous test shown in Fig. 7(b) using constant h on the entire ejector. The mean absolute errors of the Mach number from the present modeling results are 0.31 for constant h = 2.86 × 10^6 W/m^{2}K, 0.21 for constant h = 1.64 × 10^6 W/m^{2}K, and 0.11 for varying h_1 set as in the first test, respectively.

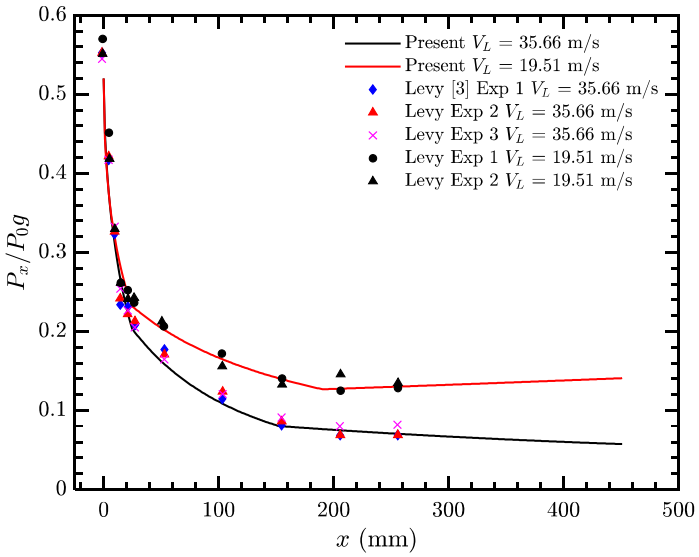

Fig. 10 Comparison of static pressure along the ejector axis with varying interfacial heat transfer coefficient and different secondary liquid flow velocities.

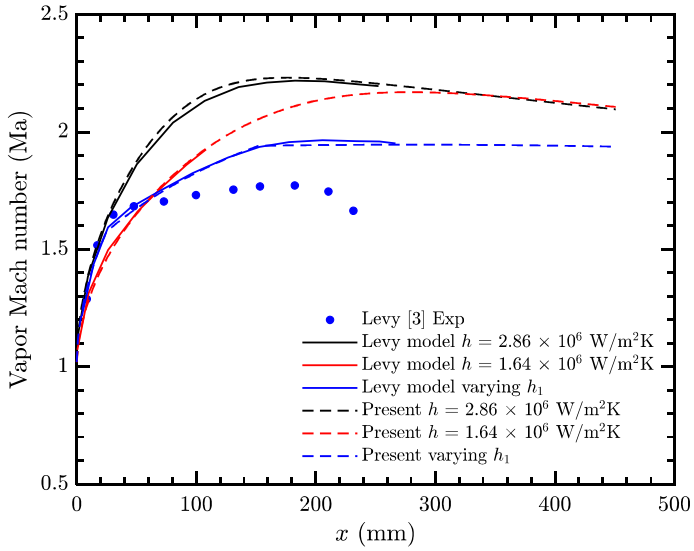

Fig. 11 Mach number distributions along the ejector axis with different interfacial heat transfer coefficient.

5.1.2 Effect of Liquid Inlet Velocity

The effects of liquid inlet velocity on static pressure, vapor and liquid temperatures, and vapor Mach number are shown in Figs. 12-14, respectively. Generally, the performance of the ejector is very similar when the liquid inlet velocity larger than 25 m/s. When V_{L0} = 12 m/s, the outlet static pressure and liquid temperature are the highest, while the vapor Mach number is the lowest among all the cases presented. In contrast, the liquid temperature is not sensitive to the liquid inlet velocity. Following the changes in the magnitude of the heat transfer coefficient along the ejector axis for the other two inlet velocity cases, the varying heat transfer coefficient h_3 for the case with V_{L0} = 12 m/s is adjusted to 2.04 MW/m^{2}K in the range $0 < x < 25.4$ mm, to 0.2 MW/m^{2}K from 25.4 < x < 152.4 mm, and to 0.002 MW/m^{2}K for $x > 152.4$ mm.

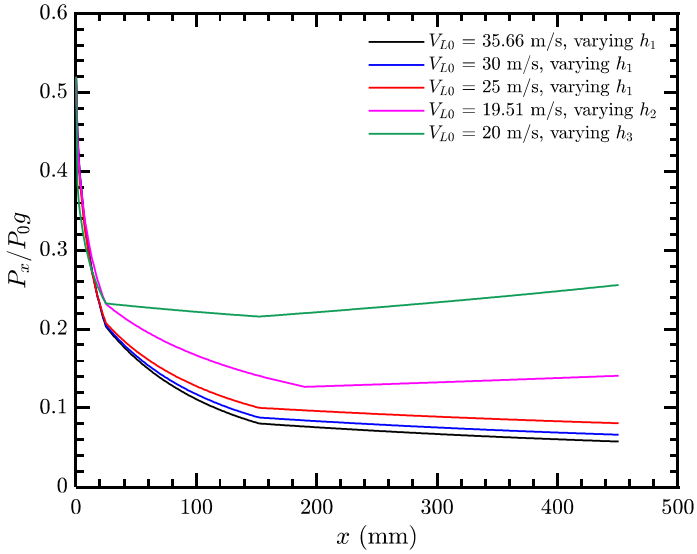

Fig. 12 Static pressure distribution along the ejector axis at different liquid inlet velocities.

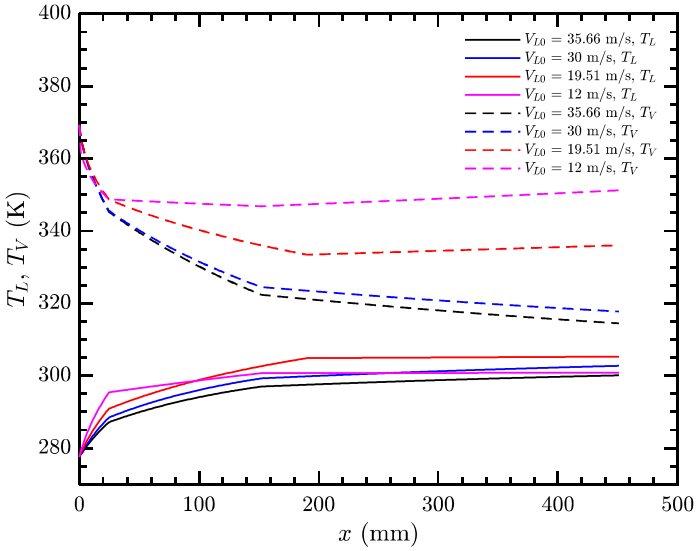

Fig. 13 Vapor and liquid temperature profiles along the ejector axis at different liquid inlet velocities.

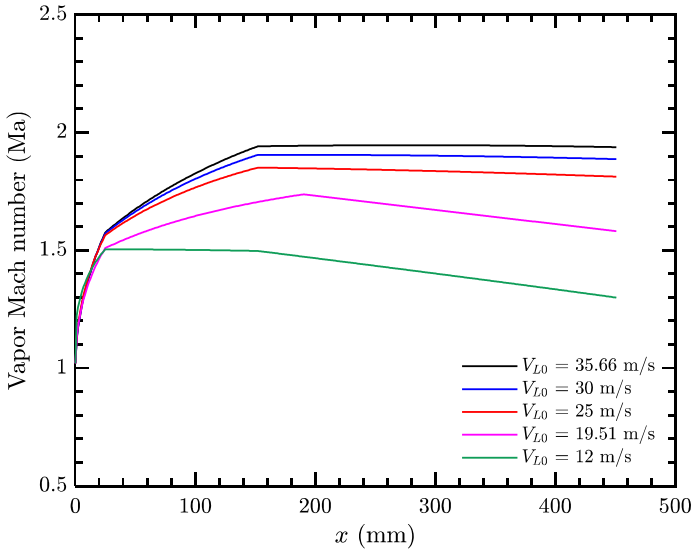

Fig. 14 Mach number distributions along the ejector axis at different liquid inlet velocities.

5.1.3 Effect of Vapor Inlet Temperature

Figs. 15-17 demonstrate the vapor inlet temperature effect on the performance of the ejector. Although the vapor inlet temperatures are different (T_{V0} = 433.15 K, 403.15 K, 383.15 K, and 373.15 K), the distributions of static pressure, vapor and liquid temperature almost overlap each other. For higher inlet liquid velocity at 35.66 m/s, it can be seen in Fig. 17 that the vapor Mach number along the ejector axis increases with vapor inlet temperature. It can also be observed from Figs. 15 and 16 that when the liquid inlet velocity is 19.51 m/s, higher static pressure and lower vapor Mach number are noticed compared to the case at V_{L0} = 35.66 m/s, which verifies the results presented in Section 5.1.2.

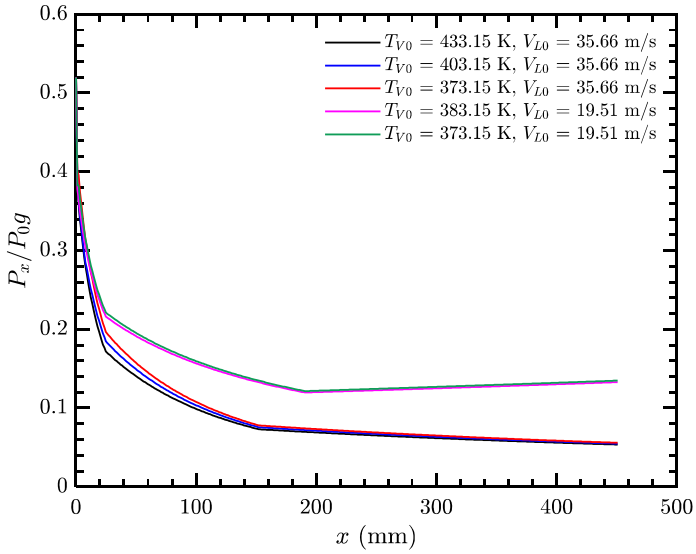

Fig. 15 Static pressure along the ejector axis at different vapor inlet temperatures.

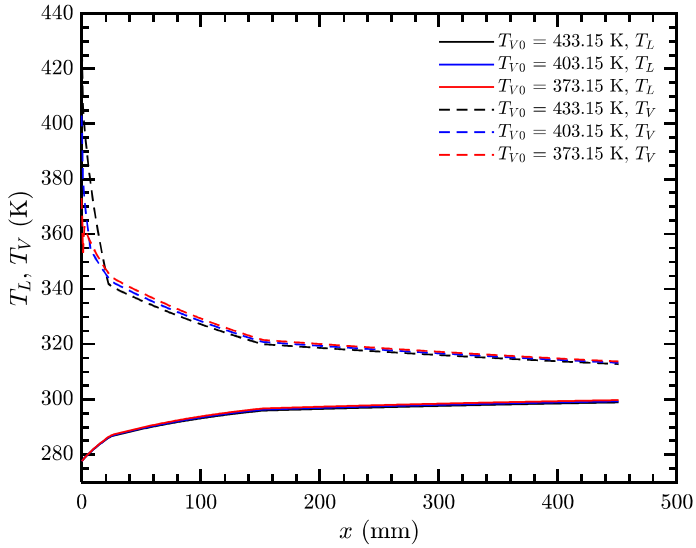

Fig. 16 Vapor and liquid temperature profiles along the ejector axis at different vapor inlet temperatures.

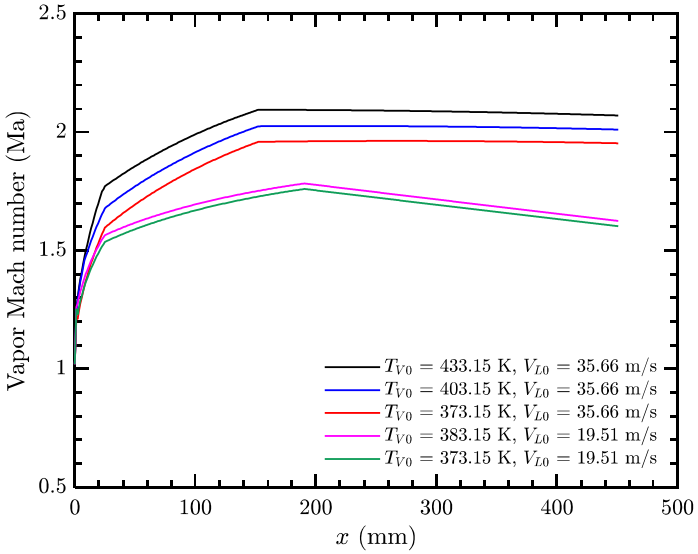

Fig. 17 Mach number distributions along the ejector axis at different vapor inlet temperatures.

5.1.4 Effect of Mixing Region Diameter

In this section, we also study the effect of the main geometric parameter, the mixing region diameter of the ejector, on its performance, and the results are shown in Figs. 18-20. It is clear that the influence of the mixing tube diameter on the static pressure, vapor and liquid temperatures, and vapor Mach number is significant. Reducing the diameter of the mixing region can make the static pressure drop faster, enhance the temperature mixing of the liquid and vapor streams through the interface, and increase the vapor Mach number.

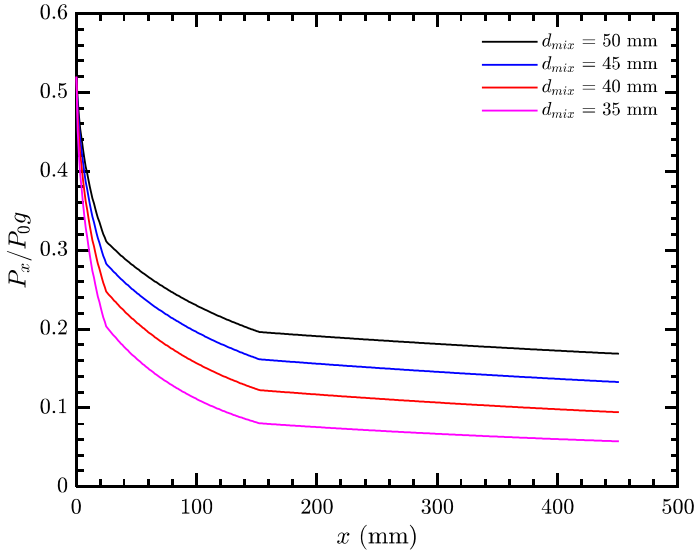

Fig. 18 Static pressure along the ejector axis with different mixing region diameters.

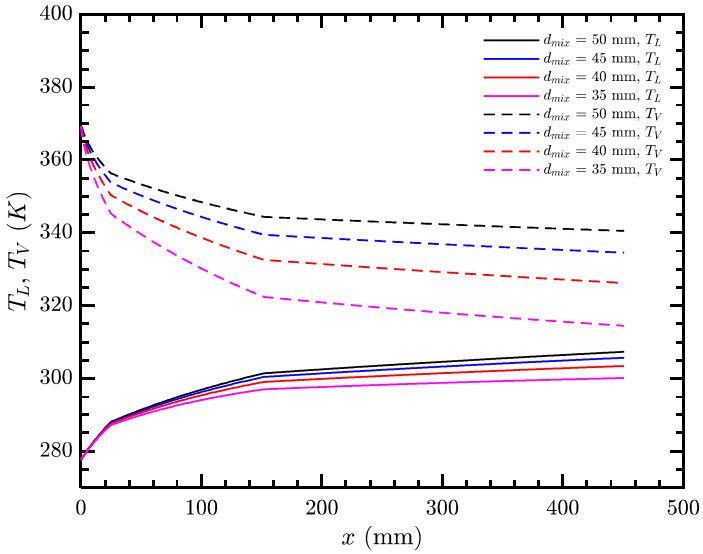

Fig. 19 Vapor and liquid temperature profiles along the ejector axis with different mixing region diameters.

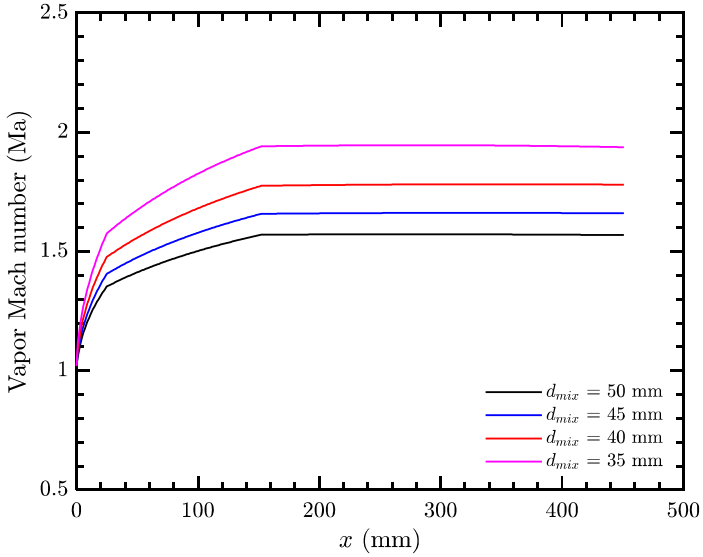

Fig. 20 Vapor Mach number distributions along the ejector axis with different mixing region diameters.

5.2 Ejectors with Primary Vapor and Secondary Liquid Flows

5.2.1 Effect of Liquid Inlet Velocity

Fig. 21 shows the effect of liquid inlet velocity (V_{L0} = 120 m/s, 90 m/s, 60 m/s, 35 m/s, and 30 m/s) on the static pressure of the Type II ejector. The other parameters are same as those in Section 4.2 with inlet liquid flow temperature T = 20 °C. The normalized static pressures are

slightly distinct in the range of $0 < x < 50$ mm, but all quickly converge to about 0.023. The comparison of the centerline vapor temperature along the ejector axis at different liquid inlet velocities are shown in Fig. 22. The trend of the four curves is very similar, so the liquid inlet velocity has little effect on the vapor temperature.

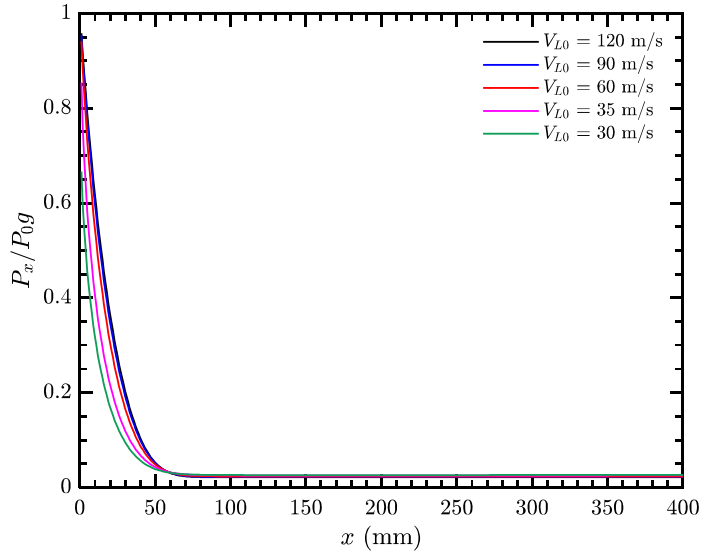

Fig. 21 Static pressure along the ejector axis at different liquid inlet velocities.

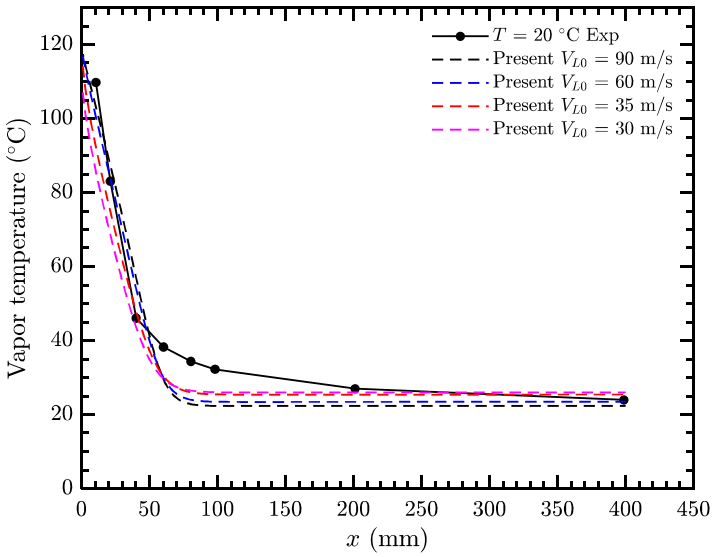

Fig. 22 Comparison of the centerline vapor temperature along the ejector axis at different liquid inlet velocities.

5.2.2 Effect of Liquid Inlet Temperature

The liquid inlet temperature effect on static pressure is demonstrated in Fig. 23. It can be seen that the different liquid inlet temperature has an obvious effect on the static pressure. The lower the secondary liquid inlet temperature, the faster the static pressure drops and the lower the outlet pressure.

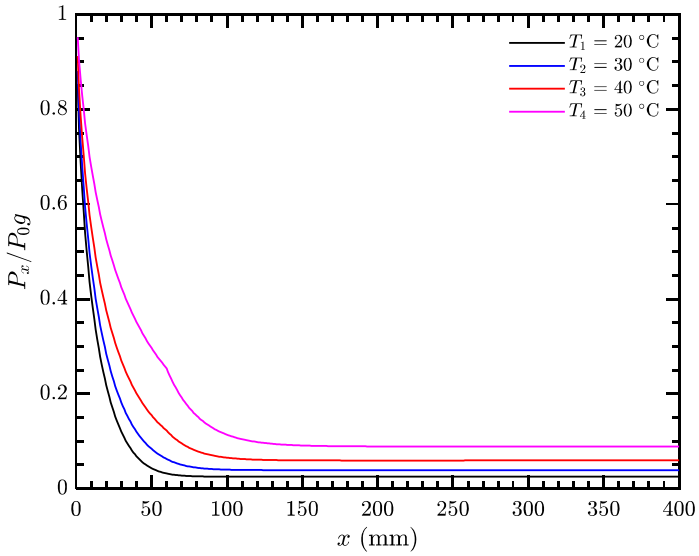

Fig. 23 Static pressure along the ejector axis at different liquid inlet temperatures.

5.2.3 Effect of Vapor Inlet Pressure

Fig. 24 shows the comparison of static pressure along the ejector axis at different vapor inlet pressure. Similar to Fig. 21, a discrepancy can be observed in the range of $0 < x < 100$ mm. The static pressure drops the slowest with P_{0g} = 380 kPa. The other two trends are similar, but all cases converge to similar values.

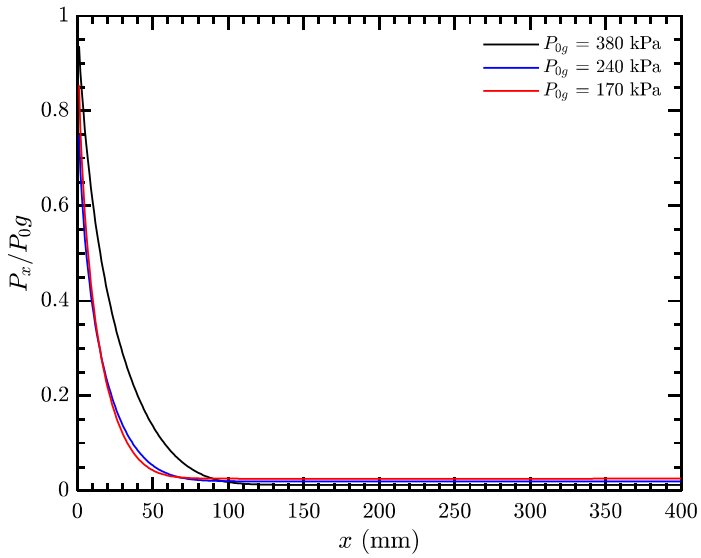

Fig. 24 Static pressure along the ejector axis at different vapor inlet pressures.

5.2.4 Effect of Mixing Region Diameter

Finally, we investigate the effect of different mixing region diameters on the performance of Type II ejector, which is shown in Fig 25. In the tested five different mixing region diameters (d_{mix} = 9.02, 8.26, 7.75, 6.48, 5.71 mm), the static pressure distribution trends are very similar, but it can still be observed that the static pressure with d_{mix} = 9.02 mm drops the fastest among all the cases.

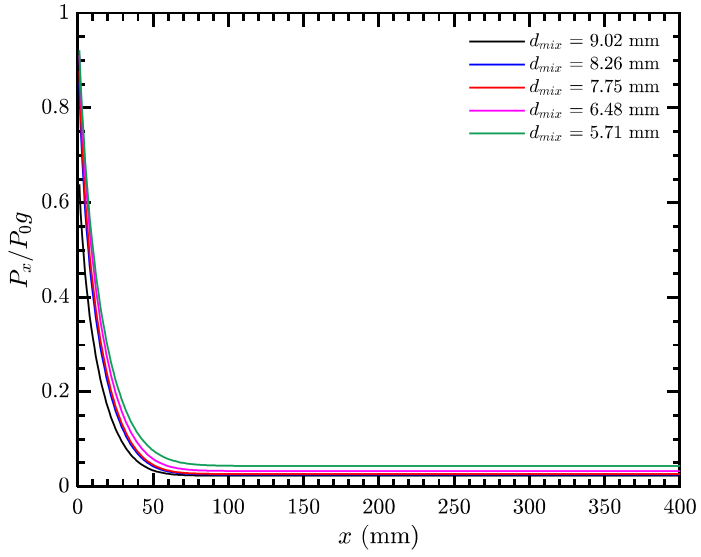

Fig. 25 Static pressure along the ejector axis with different mixing region diameters.

6. Conclusions

In this study, a 1D slug-flow model was developed and validated for condensing ejectors with both primary liquid flow (Type I) and primary vapor flow (Type II) configurations. Such simplified slug-flow models are valuable for understanding the vapor-liquid interactions in condensing ejectors and evaluating their performance when applied in refrigeration cycles and for chemical and nuclear reactors cooling. Overall, the present slug model simulation results show good agreement with published computational and experimental results in the literature. The parametric study of the generic ejectors shows that for Type I ejectors, the liquid inlet velocity and the diameter of the mixing region have significant effects on their performance, while the secondary vapor flow inlet temperature has little effect. Therefore, it is suggested to increase the liquid inlet velocity and/or decrease the mixing region diameter to improve the performance of the ejector. Different from Type I ejectors, the performance of Type II ejectors is mainly controlled by the secondary liquid flow inlet temperature and not sensitive to the changes in the liquid flow inlet velocity or the mixing region diameter. The present 1D slug-flow model can serve as an efficient and reliable tool for condensing ejectors design and optimization.

It should also be noted that based on the present work, many possible extensions and more in-depth studies can be conducted to fully investigate the vapor-liquid interactions in condensing ejectors, such as 2D axisymmetric or full 3D CFD models to provide more reliable spatially varying interfacial heat transfer coefficient, consideration of liquid jet breakup and atomization in Type I ejectors, investigation of the existence and length of condensation shocks and shock stability in both types of ejectors, and study of transitions between the distinct flow regimes in both single-phase and two-phase flows. While out of scope of this paper, those are recommended for future studies.

Acknowledgments

This material is based upon work supported by the U.S. Department of Energy's Office of Nuclear Energy under the U.S. Industry Opportunities for Advanced Nuclear Technology Development Initiative award number DE-NE0008816.

References

[1] B.M. Tashtoush, M.A. Al-Nimr, M.A. Khasawneh, A comprehensive review of ejector design, performance, and applications, Appl. Energy. (2019). https://doi.org/10.1016/j.apenergy.2019.01.185.

[2] C.K. Drummond, A Control-volume Method for Analysis of Unsteady Thrust Augmenting Ejector Flows, 1988.

[3] E.K. Levy, Investigation of Liquid-Vapor Interactions in a Constant Area Condensing Ejector, Massachusetts Institute of Technology, 1963.

[4] C.H. Song, Y.S. Kim, Direct contact condensation of steam jet in a pool, in: Adv. Heat Transf., 2011. https://doi.org/10.1016/B978-0-12-381529-3.00003-7.

[5] C.-H. Song, S. Cho, H.-S. Kang, Steam Jet Condensation in a Pool: From Fundamental Understanding to Engineering Scale Analysis, J. Heat Transfer. 134 (2012). https://doi.org/10.1115/1.4005144.

[6] C.-H. Song, S. Cho, H.-Y. Kim, Y.-Y. Bae, M.-K. Chung, CHARACTERIZATION OF DIRECT CONTACT CONDENSATION OF STEAM JETS DISCHARGING INTO A SUBCOOLED WATER, in: Proc. IAEA Tech. Comm. Meet., 1998.

[7] H.S. Kang, C.H. Song, CFD analysis for thermal mixing in a subcooled water tank under a high steam mass flux discharge condition, Nucl. Eng. Des. 238 (2008) 492–501. https://doi.org/10.1016/j.nucengdes.2007.02.044.

[8] B.J. Huang, J.M. Chang, C.P. Wang, V.A. Petrenko, 1-D analysis of ejector performance, Int. J. Refrig. 22 (1999) 354–364. https://doi.org/10.1016/S0140-7007(99)00004-3.

[9] M. Ouzzane, Z. Aidoun, Model development and numerical procedure for detailed ejector analysis and design, Appl. Therm. Eng. (2003). https://doi.org/10.1016/S1359-4311(03)00208-4.

[10] X. Wang, J. Dong, G. Zhang, Q. Fu, H. Li, Y. Han, J. Tu, The primary pseudo-shock pattern of steam ejector and its influence on pumping efficiency based on CFD approach, Energy. (2019). https://doi.org/10.1016/j.energy.2018.10.097.

[11] M. Colarossi, N. Trask, D.P. Schmidt, M.J. Bergander, Multidimensional modeling of condensing two-phase ejector flow, in: Int. J. Refrig., 2012. https://doi.org/10.1016/j.ijrefrig.2011.08.013.

[12] J.H. Keenan, E.P. Neumann, F. Lustwerk, An Investigation of Ejector Design by Analysis and Experiment, J. Appl. Mech. (1950). https://doi.org/10.1115/1.4010131.

[13] J.T. Munday, D.F. Bagster, NEW EJECTOR THEORY APPLIED TO STEAM JET REFRIGERATION., Ind Eng Chem Process Des Dev. (1977).

[14] I.W. Eames, S. Aphornratana, H. Haider, A theoretical and experimental study of a small-scale steam jet refrigerator, Int. J. Refrig. (1995). https://doi.org/10.1016/0140-7007(95)98160-M.

[15] D.W. Sun, I.W. Eames, Performance characteristics of HCFC-123 ejector refrigeration cycles, Int. J. Energy Res. (1996). https://doi.org/10.1002/(SICI)1099-114X(199610)20:10<871::AID-ER201>3.0.CO;2-4.

[16] D.W. Sun, Geometry ejectors and their applications in ejector refrigeration systems, Energy. (1996). https://doi.org/10.1016/0360-5442(96)00038-2.

[17] E.D. Rogdakis, G.K. Alexis, Design and parametric investigation of an ejector in an air-conditioning system, Appl. Therm. Eng. (2000). https://doi.org/10.1016/S1359-4311(99)00013-7.

[18] S. Varga, A.C. Oliveira, B. Diaconu, Numerical assessment of steam ejector efficiencies

using CFD, Int. J. Refrig. (2009). https://doi.org/10.1016/j.ijrefrig.2009.01.007.
[19] X. Ma, W. Zhang, S.A. Omer, S.B. Riffat, Experimental investigation of a novel steam ejector refrigerator suitable for solar energy applications, Appl. Therm. Eng. (2010). https://doi.org/10.1016/j.applthermaleng.2010.02.011.
[20] F. Liu, E.A. Groll, Study of ejector efficiencies in refrigeration cycles, Appl. Therm. Eng. (2013). https://doi.org/10.1016/j.applthermaleng.2012.12.001.
[21] K. Chunnanond, S. Aphornratana, An experimental investigation of a steam ejector refrigerator: The analysis of the pressure profile along the ejector, Appl. Therm. Eng. (2004). https://doi.org/10.1016/j.applthermaleng.2003.07.003.
[22] H. Landoulsi, M. Elakhdar, E. Nehdi, L. Kairouani, Performance analysis of a combined system for cold and power, Int. J. Refrig. (2015). https://doi.org/10.1016/j.ijrefrig.2015.07.033.
[23] B. Tashtoush, A.B.R. Algharbawi, Parametric study of a Novel Hybrid Solar Variable Geometry Ejector cooling with Organic Rankine Cycles, Energy Convers. Manag. (2019). https://doi.org/10.1016/j.enconman.2019.111910.
[24] S.B. Riffat, G. Gan, S. Smith, Computational fluid dynamics applied to ejector heat pumps, Appl. Therm. Eng. (1996). https://doi.org/10.1016/1359-4311(95)00033-X.
[25] J. Dong, Q. Hu, M. Yu, Z. Han, W. Cui, D. Liang, H. Ma, X. Pan, Numerical investigation on the influence of mixing chamber length on steam ejector performance, Appl. Therm. Eng. (2020). https://doi.org/10.1016/j.applthermaleng.2020.115204.
[26] J. Keenan, F. Keyes, Thermodynamic properties of steam, John Wiley and Sons, Inc., 1936.